

Sound Field Reconstruction Using a Compact Acoustics-informed Neural Network

Fei Ma,¹ Sipei Zhao,^{1, a} and Ian S. Burnett²

¹Center for Audio, Acoustics and Vibration, Faculty of Engineering and IT, University of Sydney Technology, Ultimo, NSW 2007, Australia.

²DVC and VP STEM, RMIT University, Melbourne, VIC 3000, Australia

(Dated: 15 February 2024)

Sound field reconstruction (SFR) augments the information of a sound field captured by a microphone array. Conventional SFR methods using basis function decomposition are straightforward and computationally efficient, but may require more microphones than needed to measure the sound field. Recent studies show that pure data-driven and learning-based methods are promising in some SFR tasks, but they are usually computationally heavy and may fail to reconstruct a physically valid sound field. This paper proposes a compact acoustics-informed neural network (AINN) method for SFR, whereby the Helmholtz equation is exploited to regularize the neural network. As opposed to pure data-driven approaches that solely rely on measured sound pressures, the integration of the Helmholtz equation improves robustness of the neural network against variations during the measurement processes and prompts the generation of physically valid reconstructions. The AINN is designed to be compact, and is able to predict not only the sound pressures but also sound pressure gradients within a spatial region of interest based on measured sound pressures along the boundary. Numerical experiments with acoustic transfer functions measured in different environments demonstrate the superiority of the AINN method over the traditional cylinder harmonic decomposition and the singular value decomposition methods.

[<https://doi.org/DOI number>]

[XYZ]

Pages: 1–12

I. INTRODUCTION

Microphone arrays are commonly used for measuring a sound field (Benesty *et al.*, 2008) and to maximize the information about the source, a large-aperture array with densely-spaced microphones, is preferred for sound field measurements. However, that is not always possible due to practical considerations such as cost and microphone arrangement (Rafaely, 2015). This necessitates sound field reconstruction (SFR) (Fernandez-Grande, 2016; Williams, 1999; Zhang *et al.*, 2008), a task that aims to reconstruct a sound field apart from the limited (sparse) measurements.

Existing SFR methods can be broadly classified into two categories: conventional methods based on basis function decomposition and recent learning-based methods. The conventional methods decompose sound field measurements into some basis functions, such as cylinder harmonics (CHs) (Williams, 1999), spherical harmonics (Chen *et al.*, 2015; Tang *et al.*, 2022; Verburg and Fernandez-Grande, 2018; Wabnitz *et al.*, 2011; Williams, 1999), prolate spheroidal wave functions (Zhang *et al.*, 2023), plane waves (Antonello *et al.*, 2017; Fernandez-Grande, 2016; Schmid *et al.*, 2021; Williams, 1999), and their corresponding weights. The basis functions are

solutions of the Helmholtz equation (Skudrzyk, 2012; Williams, 1999), the governing partial differential equation (PDE) of acoustic wave propagation, and are continuous spatial functions which can be evaluated at arbitrary positions. These two factors make the conventional methods easy to compute and generate a physically valid reconstruction of the sound field away from the measurement positions. However, the basis functions are designed with respect to some coordinate systems (Williams, 1999) without considering the statistical characteristics of sound fields. Thus, conventional methods may require more than the absolutely necessary number of measurements (spatial sampling points) to determine the basis function weights to reconstruct a sound field. The reality is that the statistical characteristics of a sound field can be used to allow the sampling requirement to be relaxed based on singular value decomposition (SVD) (Zhu *et al.*, 2020, 2021), compressive sensing (Verburg and Fernandez-Grande, 2018; Wabnitz *et al.*, 2011), statistical learning (Hahmann *et al.*, 2021), or Bayesian inference (Schmid *et al.*, 2021).

In contrast to conventional methods, recent learning-based methods do not rely on pre-designed basis functions. Instead, they exploit the learned statistical characteristics of sound fields for SFR. Llus *et al.* (Llus *et al.*, 2020) and Kristoffersen *et al.* (Kristoffersen *et al.*, 2021) developed U-net-like neural networks, which were trained with simulated or measured room impulse responses. The

^aElectronic mail: Sipei.Zhao@uts.edu.au

U-net-like neural networks achieved superior SFR performance than some of the conventional methods in the low frequency range (< 300 Hz). Hahmann *et al.* (Hahmann *et al.*, 2021) proposed to learn basis functions in local subdomains. The learned basis functions generalized across different rooms and frequencies, and showed potential for modeling complex sound fields according to their local (spatial) or statistical characteristics. By further enforcing self-similarity between adjacent local subdomains (Hahmann and Fernandez-Grande, 2022), the method attained better SFR performance when few measurements were available. Most recently, Fernandez-Grande *et al.* examined the use of generative adversarial networks for SFR (Fernandez-Grande *et al.*, 2023). The generative adversarial networks recovered some of the sound field energy at high frequencies that would otherwise be lost due to under-sampling (Fernandez-Grande *et al.*, 2023), demonstrating the promise of using statistical learning methods to overcome the sampling limitations. Although the learning-based methods outperformed the conventional methods in some SFR tasks, their computations are time-consuming. Furthermore, they are purely data-driven and thus do not necessarily reconstruct physically valid sound fields (Fernandez-Grande *et al.*, 2023).

Recently, physical laws have been integrated into neural networks for various acoustic studies, such as the Kirchhoff–Helmholtz-based convolutional neural network (CNN) for nearfield acoustic holography (Olivieri *et al.*, 2021), the physics-informed CNN (PI-CNN) for sound field estimation (Shigemi *et al.*, 2022), and the PINN for room impulse response reconstruction (Karakonstantis *et al.*, 2024; Pezzoli *et al.*, 2023). These studies (Karakonstantis *et al.*, 2024; Olivieri *et al.*, 2021; Pezzoli *et al.*, 2023; Shigemi *et al.*, 2022) attempted to reconstruct the sound field within a region of interest (ROI) with few measurements inside the ROI.

In an alternative approach, this paper proposes an acoustic-informed neural network (AINN) to reconstruct the sound field within the ROI based on the sound pressures measured on its boundary alone (Cuomo *et al.*, 2022; Raissi *et al.*, 2019). The AINN is designed to approximate the sound field at the measurement positions and is guided by the Helmholtz equation to generate physically valid reconstructions away from the measurement positions. The AINN is compact and lightweight, making it easier to train than large neural networks. In addition, owing to the automatic-differentiation of deep-learning libraries (Pezzoli *et al.*, 2023), the AINN is able to reconstruct the pressure gradient within the ROI. Numerical experiments with transfer functions measured with two microphone arrays in three different rooms (Zhao *et al.*, 2022) are conducted to compare the proposed method with the CH (Williams, 1999) and the SVD (Zhu *et al.*, 2021) methods. The experimental results demonstrate the superiority of the proposed AINN method over the existing methods.

The remainder of this paper is organized as follows. The problem is formulated in Sec. II. The CH method

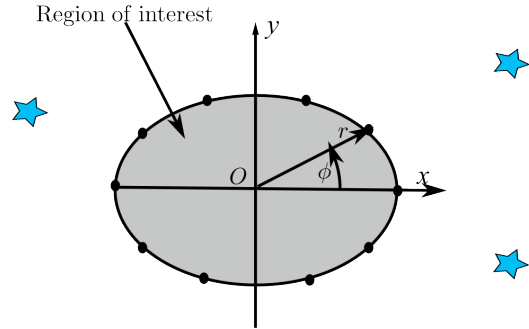


FIG. 1. (color online) Problem setup: A number of sources \star generate a sound field within a ROI, which is measured by microphones \bullet on the boundary of the ROI. The objective is to reconstruct the sound pressure and its gradient within the ROI based on the microphone measurement.

and the SVD method are reviewed in Sec. III, followed by the proposed AINN method. Numerical experiments are presented in Sec. IV to validate the performance of the proposed AINN method, in comparison to the CH and the SVD methods. Sec. V concludes this work.

II. PROBLEM FORMULATION

The problem of interest is illustrated in Fig. 1, where (x, y) and (r, ϕ) denote the Cartesian and polar coordinates with respect to the origin O , respectively. The stars denote sound sources that generate the sound field in the Region of Interest (ROI) depicted as the gray area. An array of microphones on the boundary of the ROI, shown as the dots in Fig. 1, measure the sound pressures at $\{x_q, y_q\}_{q=1}^Q$ (or $\{r_q, \phi_q\}_{q=1}^Q$) as $P(\omega, x_q, y_q)_{q=1}^Q$ (or $P(\omega, r_q, \phi_q)_{q=1}^Q$), where $\omega = 2\pi f$ is the angular frequency with f being the frequency. The objective is to estimate the sound pressures and their gradients inside the ROI based on the measured sound pressures on the boundary. Hereafter, the symbol ω is omitted in some quantities for notational simplicity.

There is no sound source inside the ROI, and hence the sound field within the ROI is governed by the homogeneous Helmholtz equation (Williams, 1999), i.e.,

$$P + \frac{1}{(\omega/c)^2} \nabla^2 P = 0, \quad (1)$$

where $c = 340$ m/s is the speed of sound, and ∇^2 denotes the Laplacian operator. In Cartesian coordinates, the Laplacian operator is given by (Williams, 1999)

$$\nabla^2 = \frac{\partial}{\partial x^2} + \frac{\partial}{\partial y^2}, \quad (2)$$

and in polar coordinates it is given by

$$\nabla^2 = \frac{\partial^2}{\partial r^2} + \frac{1}{r} \frac{\partial}{\partial r} + \frac{1}{r^2} \frac{\partial^2}{\partial \theta^2}. \quad (3)$$

In this paper, we build a compact neural network informed by the Helmholtz equation, Eq. (1), to reconstruct the sound field within the ROI based on the microphone measurements.

III. METHODOLOGY

This section first reviews the CH method (Williams, 1999) and the SVD method (Zhu *et al.*, 2021) for SFR, and subsequently proposes the AINN method.

A. The cylinder harmonics method

Acoustic quantities are expressed in polar coordinates for the ease of computing the CHs. Sound pressures can be decomposed into CHs as (Williams, 1999)

$$\mathbf{P}_M = \mathbf{J}\mathbf{A}, \quad (4)$$

where $\mathbf{P}_M = [P(r_1, \phi_1), P(r_2, \phi_2), \dots, P(r_Q, \phi_Q)]^\top$ denote the measured sound pressures at $\{r_q, \phi_q\}_{q=1}^Q$, $(\cdot)^\top$ is the transpose operation, $\mathbf{A} = [A_{-N}, A_{-N+1}, \dots, A_N]^\top$ denote the CH weights, and

$$\mathbf{J} = \begin{bmatrix} J_{-N}(\frac{\omega}{c}r_1)e^{iN\phi_1} & \dots & J_N(\frac{\omega}{c}r_1)e^{-iN\phi_1} \\ J_{-N}(\frac{\omega}{c}r_2)e^{iN\phi_2} & \dots & J_N(\frac{\omega}{c}r_2)e^{-iN\phi_2} \\ \dots & \dots & \dots \\ J_{-N}(\frac{\omega}{c}r_Q)e^{iN\phi_Q} & \dots & J_N(\frac{\omega}{c}r_Q)e^{-iN\phi_Q} \end{bmatrix}, \quad (5)$$

is a $Q \times (2N + 1)$ matrix whose entry $J_n(\frac{\omega}{c}r_q)e^{-in\phi_q}$ is the n -order cylinder harmonic (Williams, 1999) evaluated at (r_q, ϕ_q) , i is the imaginary number unit, and $J_n(\cdot)$ is the Bessel function of order n (Williams, 1999). In Eqs. (4) and (5), N is the dimensionality of the sound field under CH decomposition and is normally chosen as (Kennedy *et al.*, 2007)

$$N = \lceil 2\pi fr/c \rceil, \quad (6)$$

where $\lceil \cdot \rceil$ is the ceiling operation,

The CH method estimates the weights $\hat{\mathbf{A}} = [\hat{A}_{-N}, \hat{A}_{-N+1}, \dots, \hat{A}_N]^\top$ through

$$\hat{\mathbf{A}} = \mathbf{J}^\dagger \mathbf{P}_M, \quad (7)$$

where $(\cdot)^\dagger$ denotes the pseudo-inverse operation. The sound pressure and the radial gradient for an arbitrary position (r_e, ϕ_e) can be reconstructed as (Williams, 1999)

$$\hat{P}_{\text{CH}}(r_e, \phi_e) \approx \sum_{n=-N}^N \hat{A}_n J_n(\frac{\omega}{c}r_e)e^{-in\phi_e}, \quad (8)$$

and

$$\frac{\partial \hat{P}_{\text{CH}}(r_e, \phi_e)}{\partial r_e} \approx \frac{\omega}{c} \sum_{n=-N}^N \hat{A}_n J'_n(\frac{\omega}{c}r_e)e^{-in\phi_e}, \quad (9)$$

where $J'_n(\cdot)$ denotes the derivative of the Bessel function with respect to the argument. The pressure gradient along the x -axis and the y -axis at (x_e, y_e) can be

reconstructed as

$$\frac{\partial \hat{P}_{\text{CH}}(x_e, y_e)}{\partial x_e} = \frac{\hat{P}_{\text{CH}}(r_e, \phi_e)}{\partial r_e} \cos(\phi_e), \quad (10)$$

$$\frac{\partial \hat{P}_{\text{CH}}(x_e, y_e)}{\partial y_e} = \frac{\hat{P}_{\text{CH}}(r_e, \phi_e)}{\partial r_e} \sin(\phi_e). \quad (11)$$

B. The SVD method

The SVD method (Zhu *et al.*, 2020, 2021) regards a source at (x_s, y_s) as a cluster of virtual point sources whose positions are $\{x_{s,j}, y_{s,j}\}_{j=1}^J$ and constructs two matrices with respect to the virtual point sources. The first one is a matrix of transfer functions between the virtual point sources and the microphones

$$\mathbf{H}_{\text{SM}} = \begin{bmatrix} H(x_1, y_1, x_{s,1}, y_{s,1}) & \dots & H(x_1, y_1, x_{s,J}, y_{s,J}) \\ \dots & \dots & \dots \\ H(x_Q, y_Q, x_{s,1}, y_{s,1}) & \dots & H(x_Q, y_Q, x_{s,J}, y_{s,J}) \end{bmatrix}, \quad (12)$$

where the q -th row and j -th column entry, $H(x_q, y_q, x_{s,j}, y_{s,j})$, is the free-field transfer function (Williams, 1999) between the virtual point source located at $(x_{s,j}, y_{s,j})$ and the microphone located at (x_q, y_q) (Williams, 1999). The second one is a matrix of transfer functions between the virtual point sources and the pressure estimation points

$$\mathbf{H}_{\text{SV}} = \begin{bmatrix} H(x_1, y_1, x_{s,1}, y_{s,1}) & \dots & H(x_1, y_1, x_{s,J}, y_{s,J}) \\ \dots & \dots & \dots \\ H(x_V, y_V, x_{s,1}, y_{s,1}) & \dots & H(x_V, y_V, x_{s,J}, y_{s,J}) \end{bmatrix}, \quad (13)$$

where the v -th row and j -th column entry, $H(x_v, y_v, x_{s,j}, y_{s,j})$, is the free-space transfer function (Williams, 1999) between the virtual point source located at $(x_{s,j}, y_{s,j})$ and the pressure estimation point located at (x_v, y_v) . The two matrices are decomposed as (Zhu *et al.*, 2021)

$$\mathbf{H}_{\text{SM}} = \mathbf{U}_{\text{SM}} \mathbf{\Sigma}_{\text{SM}} \mathbf{V}_{\text{SM}}^*, \quad (14)$$

and

$$\mathbf{H}_{\text{SV}} = \mathbf{U}_{\text{SV}} \mathbf{\Sigma}_{\text{SV}} \mathbf{V}_{\text{SV}}^*, \quad (15)$$

where $(\cdot)^*$ denotes the complex conjugate operation; \mathbf{U}_{SM} and \mathbf{U}_{SV} are unitary matrices whose columns represent the basis functions of the receiver space; \mathbf{V}_{SM} and \mathbf{V}_{SV} are unitary matrices whose columns represent the basis functions of the source space; and $\mathbf{\Sigma}_{\text{SM}}$ and $\mathbf{\Sigma}_{\text{SV}}$ are diagonal matrices whose elements represent the capability of a source space basis function to excite a receiver space basis function.

The SVD method (Zhu *et al.*, 2021) reconstructs the sound pressure $\hat{\mathbf{P}}_V = [\hat{P}(x_1, y_1), \dots, \hat{P}(x_v, y_v), \dots, \hat{P}(x_V, y_V)]^\top$ as

$$\hat{\mathbf{P}}_V = \mathbf{U}_{\text{SV}} \mathbf{\Sigma}_{\text{SV}} \mathbf{V}_{\text{SV}}^* \mathbf{V}_{\text{SM}} \mathbf{\Sigma}_{\text{SM}}^{-1} \mathbf{U}_{\text{SM}}^* \mathbf{P}_M, \quad (16)$$

where $(\cdot)^{-1}$ denotes the matrix inversion operation. To reconstruct the pressure gradient, the SVD method first

reconstructs the pressure at closely spaced positions $(x_v \pm \delta_x, y_v \pm \delta_y)$, and then approximates the pressure gradient by

$$\frac{\partial \hat{P}_{\text{SVD}}(x_v, y_v)}{\partial x_v} \approx \frac{\hat{P}(x_v + \delta_x, y_v) - \hat{P}(x_v - \delta_x, y_v)}{2\delta_x}, \quad (17)$$

$$\frac{\partial \hat{P}_{\text{SVD}}(x_v, y_v)}{\partial y_v} \approx \frac{\hat{P}(x_v, y_v + \delta_y) - \hat{P}(x_v, y_v - \delta_y)}{2\delta_y}. \quad (18)$$

The radial gradient can be reconstructed as

$$\frac{\partial \hat{P}_{\text{SVD}}(r_e, \phi_e)}{\partial r_e} = \frac{\partial \hat{P}_{\text{SVD}}(x_e, y_e)}{\partial x_e} \cos(\phi_e) + \frac{\partial \hat{P}_{\text{SVD}}(x_e, y_e)}{\partial y_e} \sin(\phi_e).$$

C. The acoustic-informed neural network method

This section proposes an AINN method for SFR. Instead of using complex-valued networks (Lee *et al.*, 2022), whose training can be complicated, to model the frequency-domain complex-valued acoustic quantities, we design the AINN method using real-valued networks.

Two designs of the AINN, depending on whether the real and imaginary parts of the sound pressure are modeled separately or collaboratively, are investigated in this paper. In the first design, the real and imaginary parts of the sound pressure are modeled with a single network and with a single loss function, as shown in Fig. 2 (a). In the second design, by contrast, the real and imaginary parts of the sound pressure are modeled separately with two small networks with individual loss functions, as illustrated in Fig. 2 (b). Hereinafter, the two designs are referred to as the coupled AINN (cAINN) and decoupled AINN (dAINN), respectively.

To model both the real and imaginary parts of the sound pressure, the one network design, cAINN, should have more expressive power and hence more hidden layers or more neurons in each hidden layer (Goodfellow *et al.*, 2016). As shown in Fig. 2 (a) and (b), this will make the inter-connection between neurons of the one network design more complicated than that of the two network design, dAINN. Although in theory cAINN is capable of exploiting both the real and imaginary parts of the sound pressure for the training process and hence may achieve better SFR performance, its training is complicated and may not achieve the desired performance in practice.

As shown in Fig. 2, for both cAINN and dAINN, the inputs are the Cartesian coordinates (x, y) and the outputs are the real and imaginary parts of the reconstructed sound pressure, denoted as $\mathcal{N}^{\Re}(x, y)$ and $\mathcal{N}^{\Im}(x, y)$, respectively. Similarly to the conventional data-driven methods, a data loss is utilized to minimize the differences between the reconstructed and the measured sound pressures at the measurement locations. The data loss for the real parts of the sound pressures \mathcal{L}_d^{\Re} is given by

$$\mathcal{L}_d^{\Re} = \frac{1}{Q} \sum_{q=1}^Q (P^{\Re}(x_q, y_q) - \mathcal{N}^{\Re}(x_q, y_q))^2, \quad (19)$$

where $P^{\Re}(x_q, y_q)$ and $\mathcal{N}^{\Re}(x_q, y_q)$ denote the real parts of the measured and reconstructed sound pressure at $\{x_q, y_q\}_{q=1}^Q$, respectively.

To incorporate the acoustic information into the design of the neural network, the Helmholtz Eq. (1) is utilized to calculate an extra partial differential equation (PDE) loss. It is noted that, different from the data loss that is calculated only for the measured locations, the PDE loss is calculated for both the measured locations on the boundary and the SFR locations within the ROI. By uniformly sampling D positions within the ROI at $\{x_d, y_d\}_{d=1}^D$ and referring to Eqs. (1) and (2), the PDE loss for the real part of the sound pressure \mathcal{L}_p^{\Re} is given

$$\mathcal{L}_p^{\Re} = \frac{1}{D} \sum_{d=1}^D \left(\mathcal{N}^{\Re}(x_d, y_d) + \frac{1}{(w/c)^2} \left[\frac{\partial^2 \mathcal{N}^{\Re}(x_d, y_d)}{\partial x_d^2} + \frac{\partial^2 \mathcal{N}^{\Re}(x_d, y_d)}{\partial y_d^2} \right] \right)^2,$$

where $\mathcal{N}^{\Re}(x_d, y_d)$ denotes the real-part of the pressure reconstruction at $\{x_d, y_d\}$. The data loss and the PDE loss are combined and results in the total loss. The definitions of the imaginary-part data loss \mathcal{L}_d^{\Im} and PDE loss \mathcal{L}_p^{\Im} are similar to Eqs. (19) and (20), respectively, and are not shown for brevity.

For the cAINN in Fig. 2 (a), a single network is used to model the real and imaginary parts of the sound pressure, and there are $2N$ neurons in each hidden layer. The trainable parameters of the network are updated to minimize a single total loss function

$$\mathcal{L} = \mathcal{L}_d^{\Re} + \mathcal{L}_p^{\Re} + \mathcal{L}_d^{\Im} + \mathcal{L}_p^{\Im}. \quad (20)$$

For the dAINN in Fig. 2 (b), two independent networks are used to model the real and imaginary parts of the sound pressure, respectively, with N neurons in each hidden layer. The trainable parameters of two networks are updated to minimize the real-part loss

$$\mathcal{L}^{\Re} = \mathcal{L}_d^{\Re} + \mathcal{L}_p^{\Re}, \quad (21)$$

and the imaginary-part loss

$$\mathcal{L}^{\Im} = \mathcal{L}_d^{\Im} + \mathcal{L}_p^{\Im}, \quad (22)$$

respectively.

Once trained, the AINN method can reconstruct the sound pressure at an arbitrary position (x_e, y_e) as $\mathcal{N}(x_e, y_e) = \mathcal{N}^{\Re}(x_e, y_e) + i\mathcal{N}^{\Im}(x_e, y_e)$, or equivalent $\mathcal{N}(r_e, \phi_e)$. The sound pressure gradient at that position can be reconstructed as $\partial \mathcal{N}(x_e, y_e) / \partial x_e$ along the x direction and as $\partial \mathcal{N}(x_e, y_e) / \partial y_e$ along the y direction through differentiation on the network output. The pressure gradient along the radial direction can be reconstructed as

$$\frac{\partial \mathcal{N}(r_e, \phi_e)}{\partial r_e} = \frac{\partial \mathcal{N}(x_e, y_e)}{\partial x_e} \cos(\phi_e) + \frac{\partial \mathcal{N}(x_e, y_e)}{\partial y_e} \sin(\phi_e). \quad (23)$$

Here are comments on the AINN method and recommended configurations:

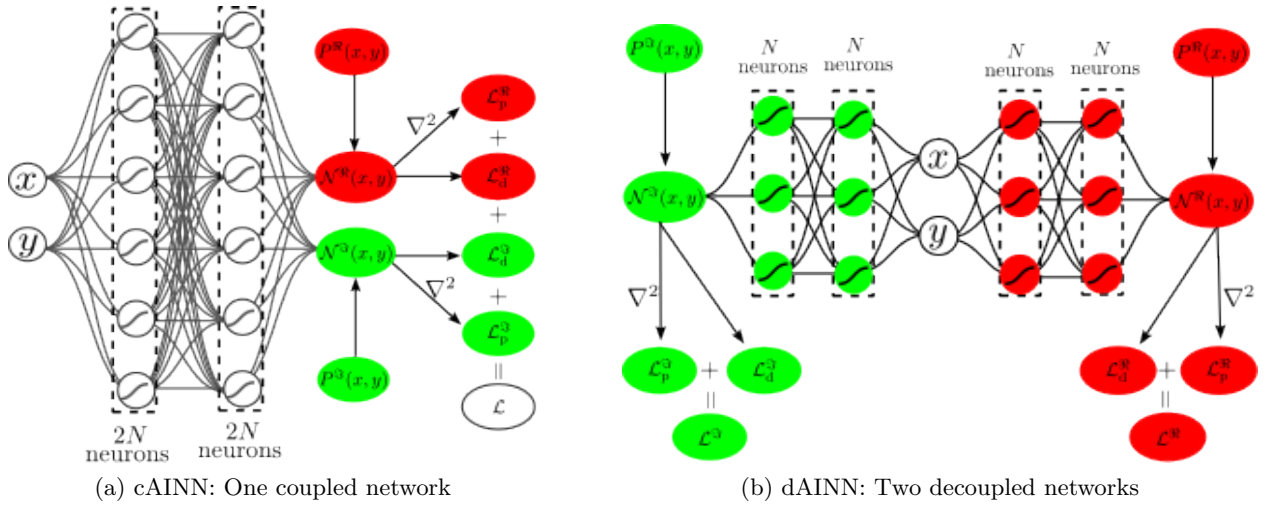


FIG. 2. (color online) Architecture of the AINN: The inputs are Cartesian coordinates, and the outputs are the real and imaginary parts of the pressure reconstruction, denoted as $\mathcal{N}^R(x, y)$ and $\mathcal{N}^I(x, y)$, respectively. The data loss and the PDE loss are calculated with respect the pressure reconstructions and its Laplacian, respectively.

1. Using tanh as the activation function:

We use tanh as the activation function for two reasons. First, the tanh function is a smooth function, whose second-order gradient can be computed. This is necessary for the Laplacian operator, Eqs. (2) and (3). Second, the tanh function outputs positive or negative values according to the input. This makes it easier to model sound pressure, whose value can be either positive or negative.

2. Cartesian coordinates vs polar coordinates:

For the AINN method, we express sound pressures in Cartesian coordinates instead of polar coordinates for two reasons. First, the presence of the $1/r$ term can make the Laplacian operator in polar coordinates, Eq. (3), to be numerically unstable. Second, for the sound field on a circle, there is no pressure variation along the radial direction. In the case, the AINN method is unable to estimate the first- and second-order radial gradient needed for calculating the Laplacian operator in polar coordinates, Eq. (3).

3. Loss function:

The loss functions, Eqs. (20), (21), and (22), consist of both the data loss and the PDE loss. The data loss prompts the network output to approximate the measured sound pressure at positions $\{x_q, y_q\}_{q=1}^Q$, which are on the boundary of the ROI as shown in Fig. 1. The PDE loss, on the other hand, regularizes the network output to conform with the Helmholtz equation at positions $\{x_d, y_d\}_{d=1}^D$ both on the boundary of and within the ROI. D should be chosen to be sufficiently large and thus the distance between adjacent positions is at most half (ideally one tenth) of the wave-length for the frequency of interest.

4. Neuron number:

As shown in Eq. (8), the sound pressure can be expressed as a linear combination of $2N + 1$ CHs $\{J_n(kr)e^{-in\phi}\}_{n=-N}^N$, which are solutions of the Helmholtz equation, Eq. (1). As shown in Fig. 2 (a) and (b), the very same sound pressure can also be expressed as a linear combination of the output of a number of neurons. This fact inspires us to set to the number of neurons in hidden layers according to the CH decomposition of the sound pressure. Specifically, for the cAINN, the one network design, the neuron number is set to be $2N$, and for the dAINN, the two network design, the neuron number is set to be N , where $N = \lceil 2\pi fr/c \rceil \approx \lceil fr/50 \rceil$. For a sound field whose size approximates the size of human heads, i.e., $r \approx 0.1$ m, $N \leq 20$ for $f \leq 10$ kHz.

As shown in Sec. IV, an AINN with two hidden layers and less than 10 neurons on each hidden layers is found to be sufficient for modeling the sound fields around two arrays. Therefore, the AINN is compact and lightweight in comparison to other learning-based methods (Fernandez-Grande *et al.*, 2023; Hahmann and Fernandez-Grande, 2022; Hahmann *et al.*, 2021; Karakonstantis *et al.*, 2024; Kristoffersen *et al.*, 2021; Lluís *et al.*, 2020; Olivieri *et al.*, 2021; Pezzoli *et al.*, 2023; Shigemi *et al.*, 2022).

IV. EXPERIMENTS

Numerical experiments were conducted to validate the performance of the proposed AINN method, and to compare it with the CH and SVD methods.

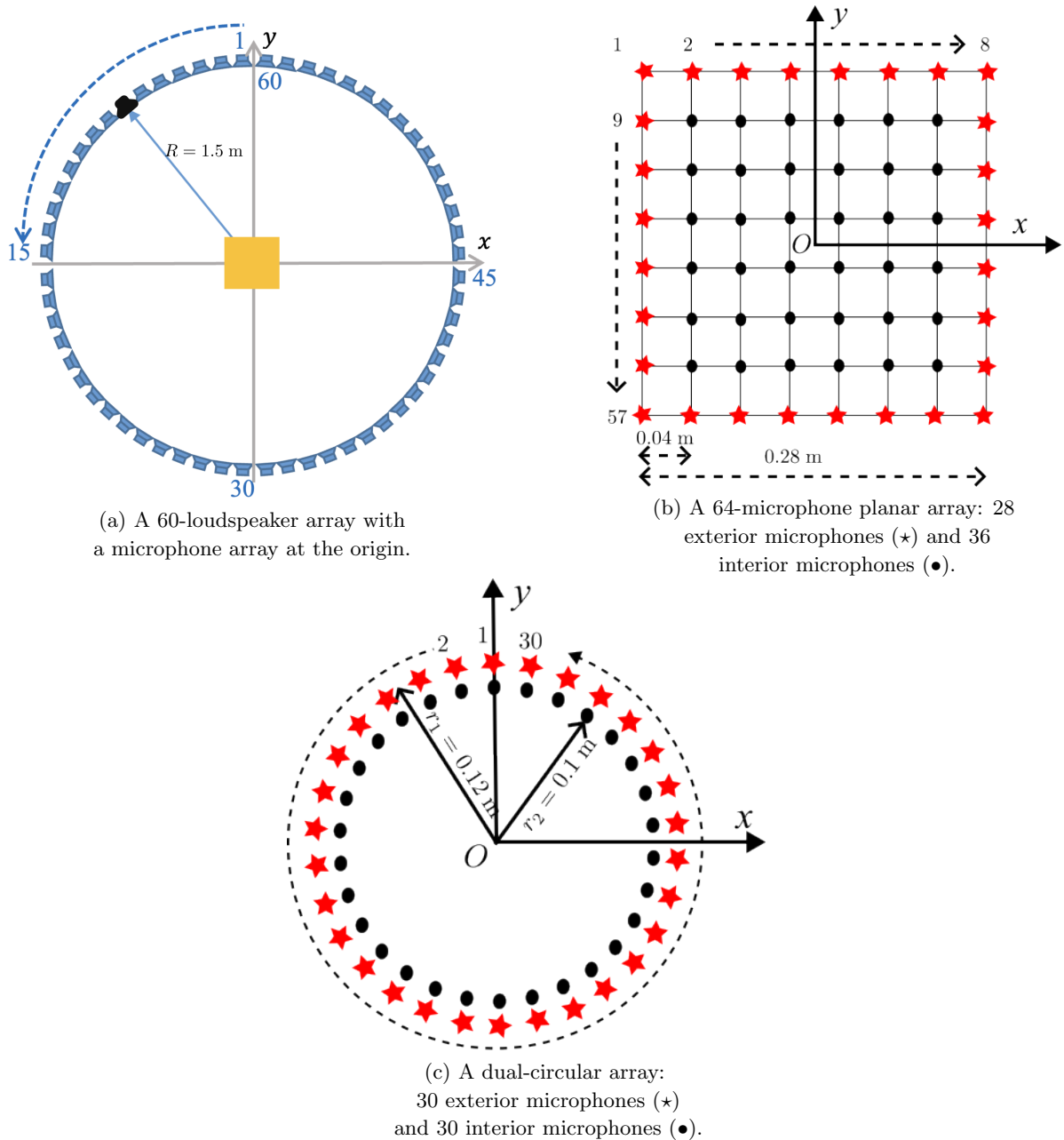


FIG. 3. (color online) Experiment setup (Zhao *et al.*, 2022): the loudspeaker array and the microphone arrays.

A. Data processing

The SFR methods were evaluated using the UTS multi-zone sound field reproduction dataset (Zhao *et al.*, 2022). The measurement set up is shown in Figs. 3 and 4. The room impulse responses (RIRs) between a loudspeaker array (Fig. 3 (a)) and two microphone arrays (Fig. 3 (b) and (c)) were measured in an anechoic chamber (Fig. 4 (a)), a medium room (Fig. 4 (b)), and a small room (Fig. 4 (c)). The loudspeaker array and the microphone arrays were arranged concentrically.

The loudspeaker array consisted of 60 Genelec 8010A Studio Monitors (Zhao *et al.*, 2022) as shown in Fig. 3

(a), and was placed approximately at the center of each room as shown in Fig. 4. The loudspeaker positions are

$$x_l = -R \sin((2l - 1)\pi/60) \text{ m}, \quad (24)$$

$$y_l = R \cos((2l - 1)\pi/60) \text{ m}, \quad (25)$$

where $l = 1, 2, \dots, 60$.

Two microphone arrays were constructed using the DPA 4060 Series Miniature Omni-directional microphones (Zhao *et al.*, 2022), which were calibrated at 1 kHz. The first array is a 64 microphone planar array with side length of 0.28 m as shown in Fig. 3 (b). The

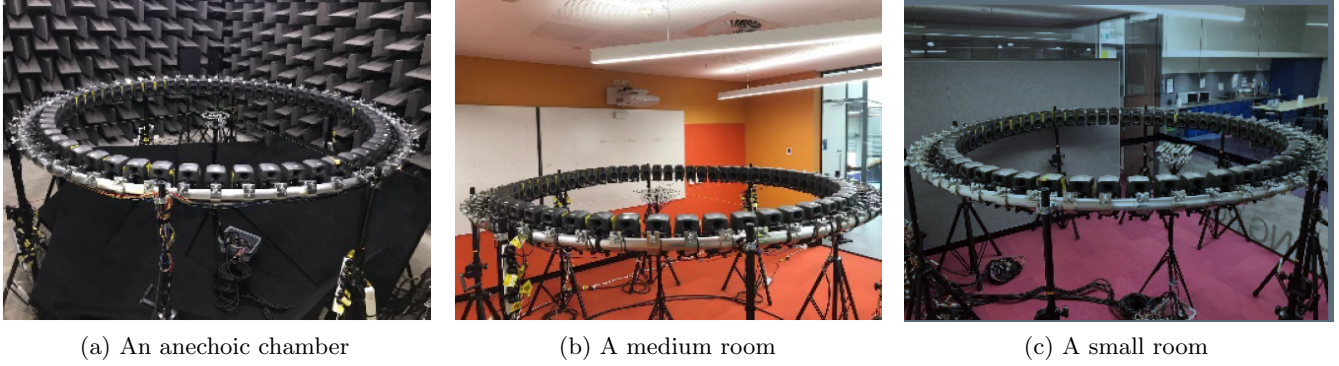


FIG. 4. (color online) Experiment setup: three room environments.

microphone positions are

$$x_m = -0.14 + 0.04 \times \text{mod}(m - 1, 8) \text{ m}, \quad (26)$$

$$y_m = 0.14 - 0.04 \times \lfloor (m - 1)/8 \rfloor \text{ m}, \quad (27)$$

where $\lfloor \cdot \rfloor$ is the floor operation, and $m = 1, 2, \dots, 64$. The second array is a dual-circular array with 30 microphones uniformly placed on each circle as shown in Fig. 3 (c). The microphone positions are

$$\theta_m = 2\pi(m - 1)/30, \quad (28)$$

$$x_m = -r \times \sin(\theta_m) \text{ m}, \quad (29)$$

$$y_m = r \times \cos(\theta_m) \text{ m}, \quad (30)$$

where $m = 1, 2, \dots, 30$, and $r = r_1 = 0.12$ m for the exterior circle and $r = r_2 = 0.1$ m for the interior circle.

The RIRs were transformed into frequency-domain transfer functions through the discrete Fourier transform (Oppenheim *et al.*, 1997), resulting in the sound pressure used for the experiments. For more details about the measurement, please refer to (Zhao *et al.*, 2022).

B. Implementation

CH method: The CH method was implemented based on Eqs. (4) - (11). Based on Eq. (6), the dimensionalities of the sound field within the planar array are $N = 3, 6, 8$ for $f = 1, 2, 3$ kHz, respectively; the dimensionalities of the sound field within the dual-circular array are $N = 3, 5, 7$ for $f = 1, 2, 3$ kHz, respectively.

SVD method: The SVD method was implemented based on Eqs. (12) - (19). For a source (loudspeaker) located at (x_s, y_s) , the virtual point sources are uniformly arranged around the source in a $0.1 \text{ m} \times 0.1 \text{ m}$ square, and the distance between two virtual point sources is 0.01 m. This amounts to 120 virtual point sources in total.

AINN method: We used the TensorFlow library, and initialized the trainable parameters according to the Xavier initialization (Glorot and Bengio, 2010). The ADAM algorithm with a learning rate of 0.001 was used as the optimizer. The AINN method was trained for 10^5

epochs. The neuron number was set based on the dimensionality of the sound field under CH decomposition. The hidden layer number was set as 1 for $f = 1$ kHz and as 2 for $f = 2, 3$ kHz based on a trial-and-error process.

The measured sound pressures at the RIO boundary and their corresponding AINN reconstructions were used for calculating the data loss. On the boundary of and within the ROI, we uniformly selected positions with a 0.01 m adjacent distance, reconstructed the sound pressures at these positions, and calculated the PDE loss with respect to them.

C. Performance metrics

The performance of all methods was evaluated by the reconstruction error

$$\xi = 10 \log_{10} \frac{\sum_{e=1}^E \|P(x_e, y_e) - \hat{P}(x_e, y_e)\|_2^2}{\sum_{e=1}^E \|P(x_e, y_e)\|_2^2}, \quad (31)$$

where $\|\cdot\|_2$ denotes the 2-norm, $P(x_e, y_e)$ and $\hat{P}(x_e, y_e)$ are the ground-truth sound pressure and its reconstruction, respectively, and $\{x_e, y_e\}_{e=1}^E$ are coordinates of the sound pressure reconstruction positions. The pressure gradient reconstruction error was defined similarly to Eq. (31).

D. Sound pressure reconstruction: loudspeaker 7

Based on the sound pressure measured by the 28 exterior microphones of the planar array (Fig. 3 (b)), we reconstructed the sound pressure at the 36 interior microphones within the array. Figs. 5, 6, and 7 show the real part of the sound pressure due to loudspeaker 7 (the black loudspeaker in Fig. 3 (a)) at 1, 2, and 3 kHz, respectively. The figures also show the reconstructions by the CH method, the SVD method, the AINN method, and corresponding (both real and imaginary parts) reconstruction errors. The results for the imaginary parts are similar and are not shown for brevity.

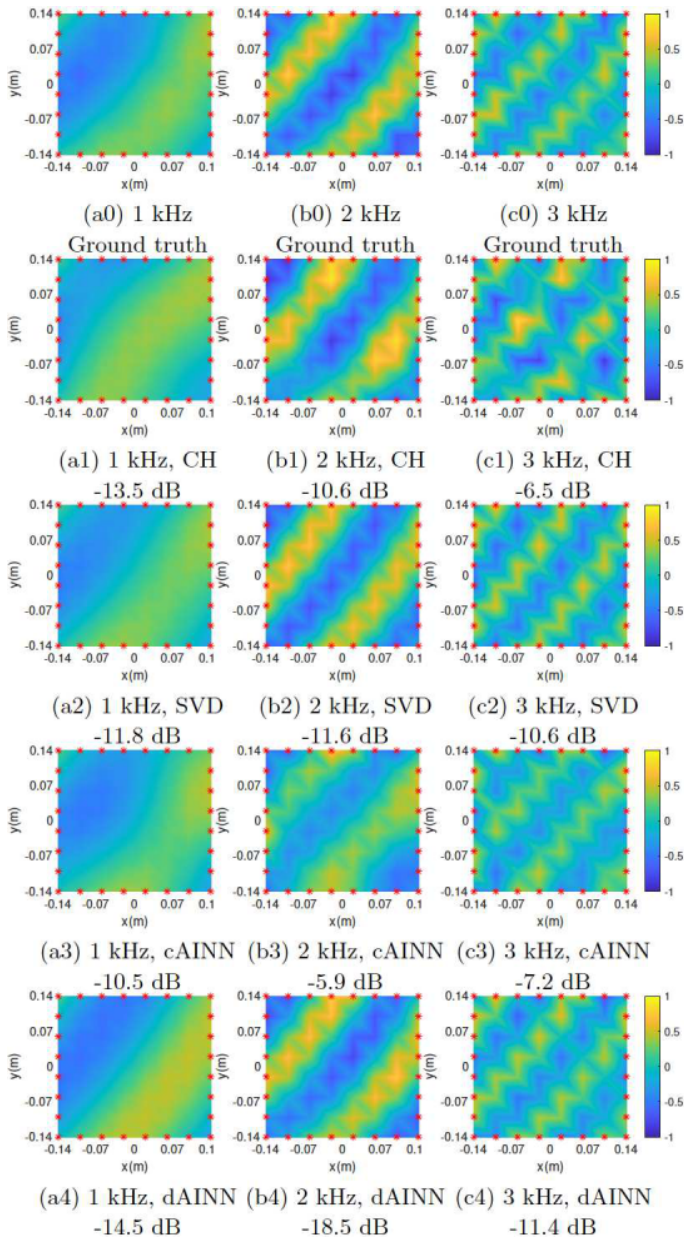


FIG. 5. (color online) Pressure reconstruction: reconstruct the pressure within the planar array based on the measured pressure (\star) - Anechoic chamber.

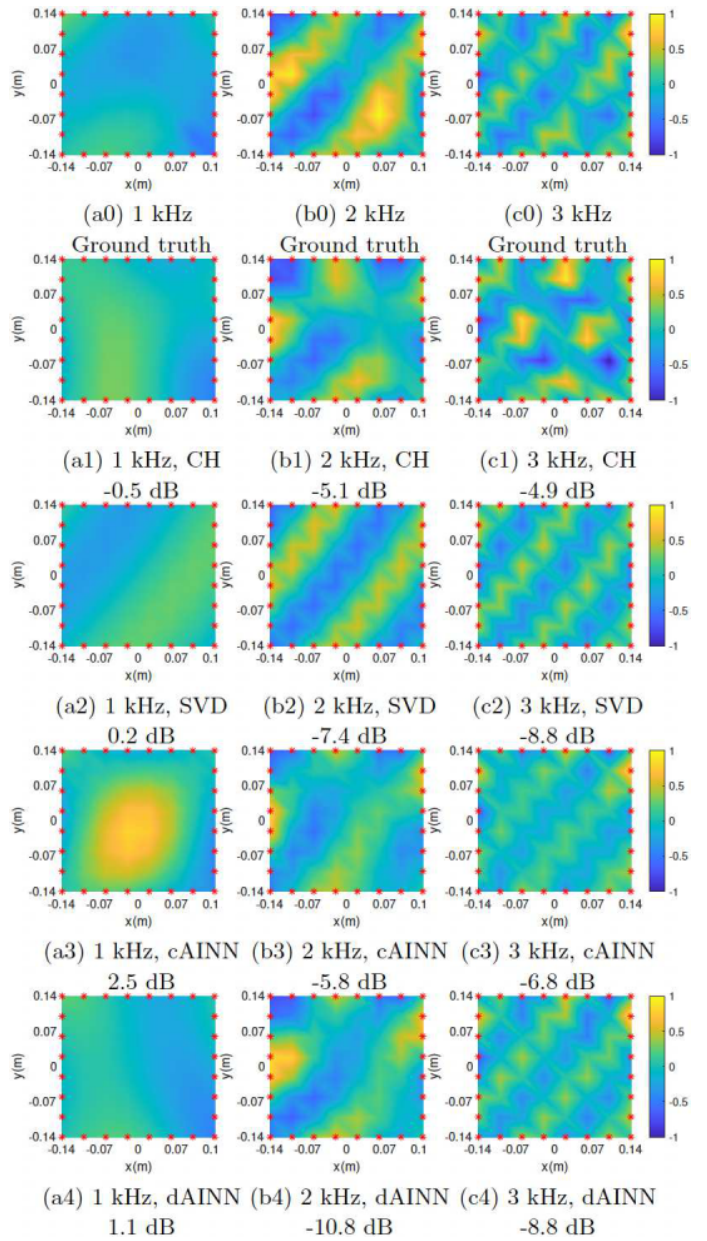


FIG. 6. (color online) Pressure reconstruction: reconstruct the pressure within the planar array based on the measured pressure (\star) - medium room.

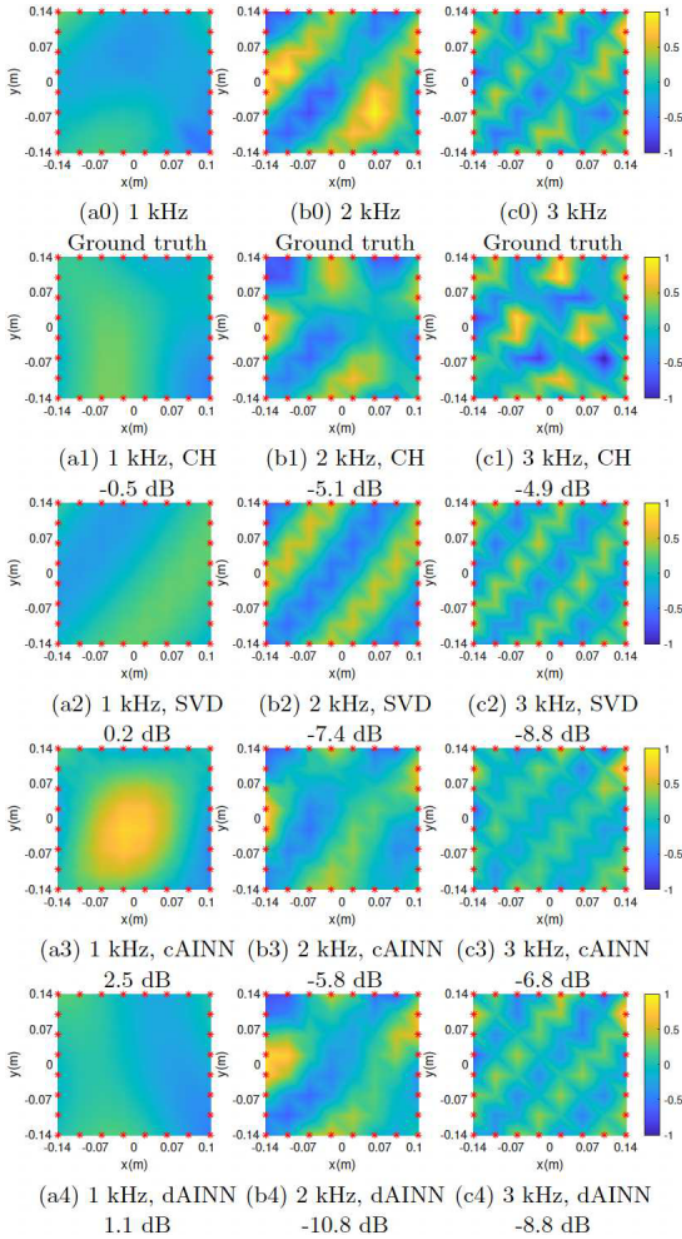


FIG. 7. (color online) Pressure reconstruction: reconstruct the pressure within the planar array based on the measured pressure (\star) - small room.

cAINN vs dAINN: As shown in Figs. 5, 6, and 7, the dAINN, two network design, outperforms the cAINN, one network design, at all frequencies and in all room environments. Experiments for the cAINN with more or less neurons on hidden layers, i.e., $\lceil 3N/2 \rceil$ or $3N$, were also conducted, and the results were also inferior to the dAINN, thus are not shown for brevity. The results demonstrate that two independent small neural networks are better than a single large neural network for modeling the real and imaginary parts of the sound pressure. Hereinafter, we focus only on the dAINN.

dAINN vs CH and SVD at 2 and 3 kHz: As shown in the second and third columns of Figs. 5, 6, and

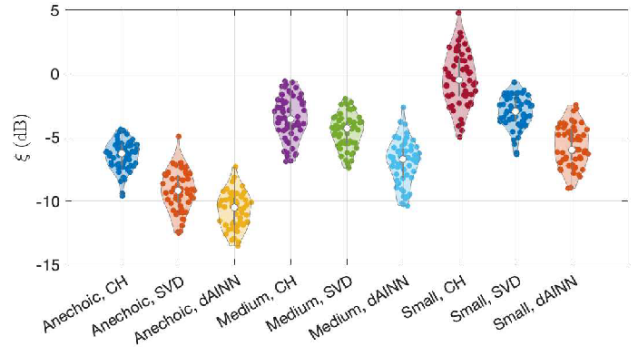


FIG. 8. (color online) Pressure reconstruction error for all loudspeakers at 3 kHz in three rooms. Small, CH denote the pressure reconstruction error of the CH method in the small room. Other labels can be interpreted similarly.

7, the SVD method performs better than the CH method and in most of the cases for $f = 2, 3$ kHz, with a decrease in the overall reconstruction error by 1.0 to 2.6 dB at 2 kHz and 1.2 to 4.1 dB 3 kHz across the three rooms. This is because the prior information of the sound source location was used in the SVD method (Zhu *et al.*, 2020, 2021). In contrast, the dAINN outperforms the SVD method in all the tested rooms at $f = 2, 3$ kHz, though no prior information about the sound source location was required by the dAINN method. This could be attributed to the fact that the CH and SVD methods relied on only the sound pressures measured on the edge of the planar array for SFR. The measured pressures did not necessarily contain sufficient information to fully determine the sound field within the planar array. The dAINN, on the other hand, exploited the Helmholtz equation for regularizing the SFR within the array through the PDE loss and reconstructed the sound field within the planar array more accurately.

Pressure variation at 1 kHz: As shown in the first column of Figs. 5, 6, and 7, at 1 kHz all methods achieve lower than -10 dB reconstruction errors in the anechoic chamber, but not in the medium room and the small room. This could be attributed the fact that at 1 kHz in the medium (Fig. 6 (a0)) and the small rooms (Fig. 7 (a0)), the pressure variations on the edge of the planar array were so small that the microphones were unable to capture enough information of the sound field, and thus the methods were unable to accurately reconstruct the sound field.

E. Sound pressure reconstruction: all loudspeakers

The SFR experiment was repeated over all the 60 loudspeakers. We set each loudspeaker to the planar array's transfer function as the ground truth, and used the sound pressure measured by the exterior 28 microphones to reconstruct the sound pressure at the interior 36 microphones within the planar array. Fig. 8 compares the sound pressure reconstruction errors of the CH, SVD, and

dAINN methods in the three rooms for all loudspeakers at 3 kHz.

Fig. 8 shows that the reconstruction errors in the anechoic chamber are smaller than those in other two rooms, as expected, due to the simpler pattern of the sound field. The dAINN achieves the smallest average reconstruction errors of -12.5, -8, and -7.2 dB, in the anechoic chamber, the medium room, and the small room, respectively. Similar experiments were also conducted at 1 kHz and 2 kHz. Except that the reconstruction errors were larger for the medium room and the small room at 1 kHz the results were similar to Fig. 8, thus are not shown here for brevity.

F. Pressure gradient reconstruction: loudspeaker 7

The sound pressures measured by the 30 microphones on the exterior circle of the dual-circular array (Fig. 3 (c)) were used to reconstruct the radial pressure gradients between the two circles. The ground truth radial pressure gradients could not be directly measured by the set up shown in Figs. 3 and 4, thus were approximated as

$$\frac{\partial P(r, \theta_m)}{\partial r} \approx \frac{P(r_1, \theta_m) - P(r_2, \theta_m)}{r_1 - r_2}, \quad (32)$$

where $m = 1, 2, \dots, 30$. The radial pressure gradients were reconstructed by the CH method, the SVD method and the dAINN method through Eq. (9), Eq. (19), and Eq. (23), respectively.

Except using the measured sound pressures to reconstruct the pressure gradient, we conducted one more numerical experiment using simulated data. The transfer functions between loudspeaker 7 and the dual-circular array were simulated using the free-field Green's function (Williams, 1999) with added white Gaussian noise at a signal-to-noise (SNR) ratio of 20 dB to model disturbances. The reconstruction errors are shown in Fig. 9. As shown in Fig. 9 (a1), (b1), and (c1), the reconstruction errors of three methods are relatively small, i.e., < -10 dB, when using the simulated sound pressures for reconstruction.

However, as shown in Fig. 9 (a2) - (c4), when the measured sound pressures, which are expected to have more measurement noises, are used, the reconstruction errors of all the three methods show signs of degradation. The data-dependent CH and SVD methods exhibit significant deviations from the ground truth in the medium room and the small room. In contrast, by exploiting the data-independent Helmholtz equation for regularization, the dAINN method is less susceptible to the inherent disturbances of the measurement processes. Thus, the dAINN method achieves the least pressure gradient reconstruction errors in most of the cases.

G. Pressure gradient reconstruction: all loudspeakers

The pressure gradient reconstruction experiment was repeated over all 60 loudspeakers. We set each loud-

speaker to the dual-circular array's transfer function as the sound pressure, approximated the radial pressure gradient according to Eq. (32), and reconstructed the pressure gradient in the same way as in Sec. IV F.

Fig. 10 shows reconstruction errors for all loudspeakers in the three rooms by the CH, SVD, and dAINN methods at 3 kHz. The experimental results for 1 and 2 kHz showed similar results as Fig. 10, thus are not shown for brevity. Comparing Fig. 10 with Fig. 8, we can see that the pressure gradient is more challenging to reconstruct than the sound pressure. The dAINN achieves the smallest average reconstruction errors of -11.5, -7.0, and -5.5 dB, in the anechoic chamber, the medium room, and the small room, respectively. The average reconstruction errors of the SVD method are about 2 dB higher than those of the dAINN. The reconstruction errors of the CH method are the worst, which exceed 0 dB in the small room.

It is noted that, in this paper, the pressure gradient was approximated by the finite difference, Eq. (32). This may not be accurate in some circumstances and may contribute to the relatively high reconstruction errors shown in Figs. 9 and 10. The velocity sensor (De Bree *et al.*, 2003) may be used for measuring the pressure gradient and testing the performance of the pressure gradient reconstruction in the future.

V. CONCLUSION

This paper proposed a compact AINN method for SFR. A neural network was designed to approximate the measured sound pressure and obey the Helmholtz equation, which regularized the network to generate physically valid output at and beyond the measurement positions. The performance of the AINN method was validated by sound pressure and pressure gradient reconstruction experiments, and outperformed both the CH and SVD methods. An extension of this work is to exploit knowledge of the sound source(s) to further improve the performance of the AINN method; this will be our topic for future work.

- Antonello, N., De Sena, E., Moonen, M., Naylor, P. A., and Van Waterschoot, T. (2017). "Room impulse response interpolation using a sparse spatio-temporal representation of the sound field," *IEEE/ACM Transactions on Audio, Speech, and Language Processing* **25**(10), 1929–1941.
- Benesty, J., Chen, J., and Huang, Y. (2008). *Microphone array signal processing*, **1** (Springer Science & Business Media).
- Chen, H., Abhayapala, T. D., and Zhang, W. (2015). "Theory and design of compact hybrid microphone arrays on two-dimensional planes for three-dimensional soundfield analysis," *The Journal of the Acoustical Society of America* **138**(5), 3081–3092.
- Cuomo, S., Di Cola, V. S., Giampaolo, F., Rozza, G., Raissi, M., and Piccialli, F. (2022). "Scientific machine learning through physics-informed neural networks: Where we are and what's next," *Journal of Scientific Computing* **92**(3), 88.
- De Bree, H.-E. *et al.* (2003). "The microflow: An acoustic particle velocity sensor," *Acoustics Australia* **31**(3), 91–94.
- Fernandez-Grande, E. (2016). "Sound field reconstruction using a spherical microphone array," *The Journal of the Acoustical Society of America* **139**(3), 1168–1178.

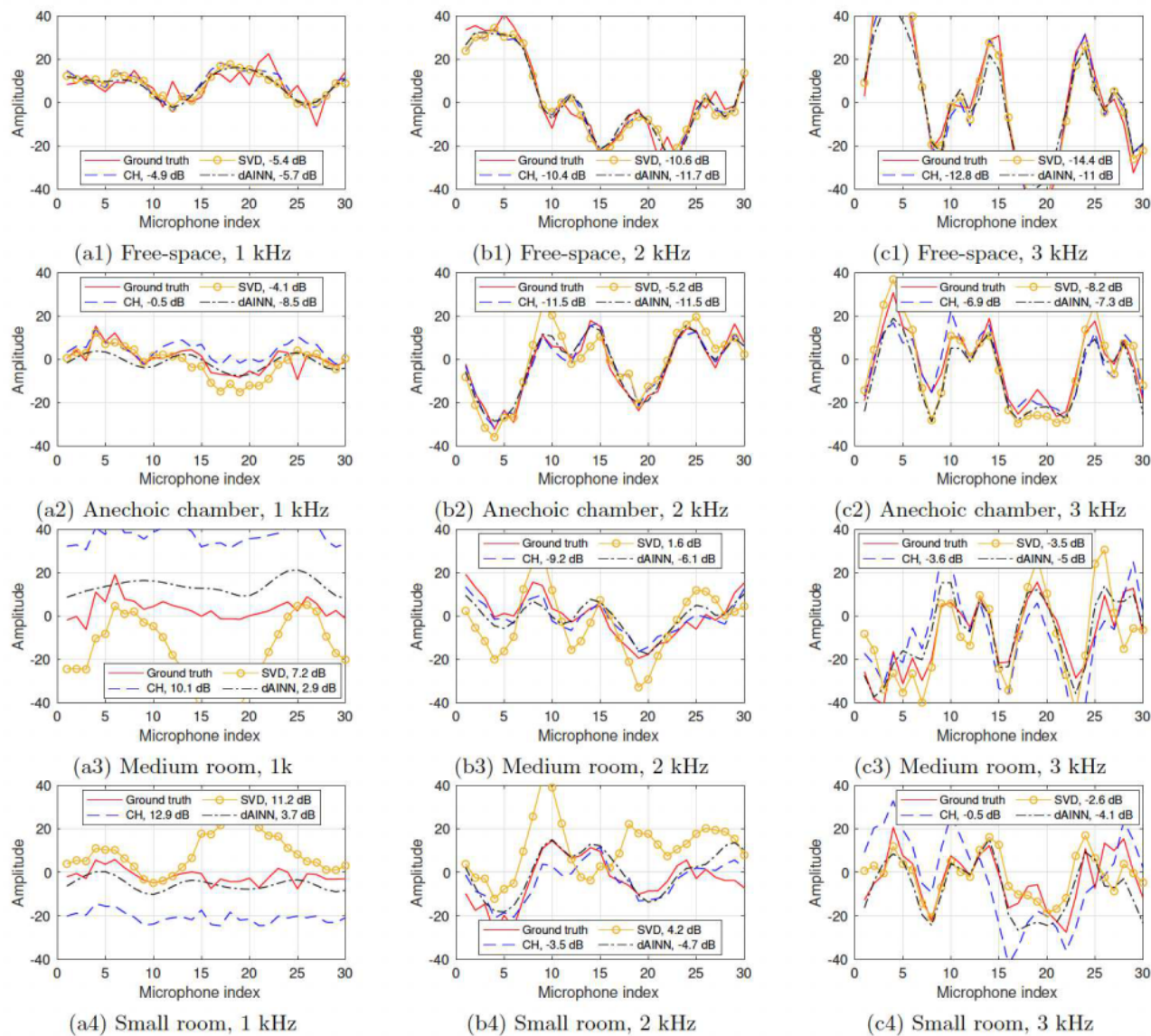


FIG. 9. (color online) Pressure gradient reconstruction: reconstruct the radial pressure gradient based the measurement of 30 microphones in the exterior circle of the dual-circular array - Loudspeaker 7. The numbers in each sub-figures denote the reconstruction errors by the SH, SVD, and dAINN methods.

Fernandez-Grande, E., Karakonstantis, X., Caviedes-Nozal, D., and Gerstoft, P. (2023). “Generative models for sound field reconstruction,” *The Journal of the Acoustical Society of America* **153**(2), 1179–1190.

Glorot, X., and Bengio, Y. (2010). “Understanding the difficulty of training deep feedforward neural networks,” in *Proceedings of the thirteenth international conference on artificial intelligence and statistics*, JMLR Workshop and Conference Proceedings, pp. 249–256.

Goodfellow, I., Bengio, Y., and Courville, A. (2016). *Deep learning* (MIT press).

Hahmann, M., and Fernandez-Grande, E. (2022). “A convolutional plane wave model for sound field reconstruction,” *The Journal of the Acoustical Society of America* **152**(5), 3059–3068.

Hahmann, M., Verburg, S. A., and Fernandez-Grande, E. (2021). “Spatial reconstruction of sound fields using local and data-driven functions,” *The Journal of the Acoustical Society of America* **150**(6), 4417–4428.

Karakonstantis, X., Caviedes-Nozal, D., Richard, A., and Fernandez-Grande, E. (2024). “Room impulse response reconstruction with physics-informed deep learning,” arXiv preprint arXiv:2401.01206 .

Kennedy, R. A., Sadeghi, P., Abhayapala, T. D., and Jones, H. M. (2007). “Intrinsic limits of dimensionality and richness in random multipath fields,” *IEEE Transactions on Signal Processing* **55**(6), 2542–2556, doi: [10.1109/TSP.2007.893738](https://doi.org/10.1109/TSP.2007.893738).

Kristoffersen, M. S., Møller, M. B., Martínez-Nuevo, P., and Østergaard, J. (2021). “Deep sound field reconstruction in real rooms: Introducing the isobel sound field dataset,” arXiv preprint arXiv:2102.06455 .

Lee, C., Hasegawa, H., and Gao, S. (2022). “Complex-valued neural networks: A comprehensive survey,” *IEEE/CAA Journal of Automatica Sinica* **9**(8), 1406–1426.

Lluis, F., Martínez-Nuevo, P., Bo Møller, M., and Ewan Shepherson, S. (2020). “Sound field reconstruction in rooms: Inpainting meets super-resolution,” *The Journal of the Acoustical Society of America*.

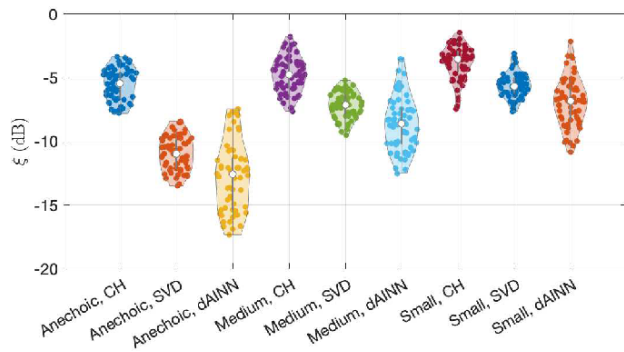


FIG. 10. (color online) Pressure gradient reconstruction error for all loudspeakers at 3 kHz in three rooms. Small, CH denote the pressure gradient reconstruction error of the CH method in the small room. Other labels can be interpreted similarly.

ety of America **148**(2), 649–659.

Olivieri, M., Pezzoli, M., Antonacci, F., and Sarti, A. (2021). “A physics-informed neural network approach for nearfield acoustic holography,” *Sensors* **21**(23), 7834.

Oppenheim, A. V., Willsky, A. S., Nawab, S. H., and Ding, J.-J. (1997). *Signals and systems*, **2** (Prentice hall Upper Saddle River, NJ).

Pezzoli, M., Antonacci, F., and Sarti, A. (2023). “Implicit neural representation with physics-informed neural networks for the reconstruction of the early part of room impulse responses,” arXiv preprint arXiv:2306.11509.

Rafaely, B. (2015). *Fundamentals of spherical array processing*, **8** (Springer).

Raissi, M., Perdikaris, P., and Karniadakis, G. E. (2019). “Physics-informed neural networks: A deep learning framework for solving forward and inverse problems involving nonlinear partial differential equations,” *Journal of Computational physics* **378**, 686–707.

Schmid, J. M., Fernandez-Grande, E., Hahmann, M., Gurbuz, C., Eser, M., and Marburg, S. (2021). “Spatial reconstruction of the sound field in a room in the modal frequency range using bayesian inference,” *The Journal of the Acoustical Society of America* **150**(6), 4385–4394.

Shigemi, K., Koyama, S., Nakamura, T., and Saruwatari, H. (2022). “Physics-informed convolutional neural network with bicubic spline interpolation for sound field estimation,” in *2022 International Workshop on Acoustic Signal Enhancement (IWAENC)*, IEEE, pp. 1–5.

Skudrzyk, E. (2012). *The foundations of acoustics: basic mathematics and basic acoustics* (Springer Science & Business Media).

Tang, X., Zhang, J., Alon, D. L., Ben-Hur, Z., Samarasinghe, P., and Abhayapala, T. (2022). “Wave domain sound field interpolation using two spherical microphone arrays,” in *2022 30th European Signal Processing Conference (EUSIPCO)*, IEEE, pp. 319–323.

Verburg, S. A., and Fernandez-Grande, E. (2018). “Reconstruction of the sound field in a room using compressive sensing,” *The Journal of the Acoustical Society of America* **143**(6), 3770–3779.

Wabnitz, A., Epain, N., van Schaik, A., and Jin, C. (2011). “Time domain reconstruction of spatial sound fields using compressed sensing,” in *2011 IEEE International Conference on Acoustics, Speech and Signal Processing (ICASSP)*, IEEE, pp. 465–468.

Williams, E. G. (1999). *Fourier acoustics: sound radiation and nearfield acoustical holography* (Academic press).

Zhang, W., Kennedy, R. A., and Abhayapala, T. D. (2008). “Iterative extrapolation algorithm for data reconstruction over sphere,” in *2008 IEEE International Conference on Acoustics, Speech and Signal Processing*, IEEE, pp. 3733–3736.

Zhang, X., Lou, J., Zhu, S., Lu, J., and Li, R. (2023). “Sound field reconstruction using prolate spheroidal wave functions and

sparse regularization,” *Sensors* **23**(19), 8312.

Zhao, S., Zhu, Q., Cheng, E., and Burnett, I. S. (2022). “A room impulse response database for multizone sound field reproduction (1),” *The Journal of the Acoustical Society of America* **152**(4), 2505–2512.

Zhu, Q., Qiu, X., Coleman, P., and Burnett, I. (2020). “A comparison between two modal domain methods for personal audio reproduction,” *The Journal of the Acoustical Society of America* **147**(1), 161–173.

Zhu, Q., Qiu, X., Coleman, P., and Burnett, I. (2021). “An experimental study on transfer function estimation using acoustic modelling and singular value decomposition,” *The Journal of the Acoustical Society of America* **150**(5), 3557–3568.